Dual photo-enhanced interpenetrating network hydrogel with biophysical and biochemical signals for infected bone defect healing

Guangyu Jian
Stomatological Hospital of Chongqing Medical University
Dize Li
Stomatological Hospital of Chongqing Medical University
Qiwei Ying
Dalian University of Technology
Xu Chen
Stomatological Hospital of Chongqing Medical University
Qiming Zhai
Stomatological Hospital of Chongqing Medical University
Si Wang
Stomatological Hospital of Chongqing Medical University
Li Mei
University of Otago
Richard D. Cannon
University of Otago
Ping Ji
Stomatological Hospital of Chongqing Medical University
Huanan Wang
Dalian University of Technology
Tao Chen (chentao1985@hospital.cqmu.edu.cn)
Stomatological Hospital of Chongqing Medical University

Research Article

Keywords: Spatiotemporal regulation, Hybrid hydrogel, Antibacterial, Immunomodulation, Bioactive ions

Posted Date: February 6th, 2023

DOI: https://doi.org/10.21203/rs.3.rs-2534216/v1

Abstract

The healing of infected bone defects (IBD) is a complex physiological process involving a series of spatially and temporally overlapping events, including pathogen clearance, immunological modulation, vascularization and osteogenesis. Based on the theory that bone healing is regulated by both biochemical and biophysical signals, in this study, we developed a copper doped bioglass (CuBGs)/methacryloyl-modified gelatin nanoparticle (MA-GNPs)/methacrylated silk fibroin (SilMA) hybrid hydrogel to promote IBD healing. This hybrid hydrogel demonstrated a dual-photocrosslinked interpenetrating network mechanism, wherein the photocrosslinked SilMA as the main network ensured structural integrity, and the photocrosslinked MA-GNPs colloidal network increased strength and dissipated loading forces. In an IBD model, the hydrogel exhibited excellent biophysical characteristics, such as adhesion, adaptation to irregular defect shapes, and *in situ* physical reinforcement. At the same time, by sequentially releasing biological biomimetic signals such as Cu^{2+}, Ca^{2+}, and Si^{2+} ions from CuBGs on demand, the hydrogel spatiotemporally coordinated antibacterial, immunomodulatory and bone remodeling events, efficiently removing infection and accelerating bone repair without the use of antibiotics or exogenous recombinant proteins. Therefore, the hybrid hydrogel can be used as a simple and effective method for the treatment of IBD.

1. Introduction

Infected bone defects (IBDs), characterized by a protracted infection and bad prognosis, are frequently encountered during orthopedic, oral, and maxillofacial surgery. The healing of IBD is a complex physiological process involving a series of spatially and temporally overlapping events, including pathogen clearance, immunological modulation, vascularization and osteogenesis[1]. The existing challenges to the healing of IBD mainly come from two aspects. On the one hand, the emergence of drug-resistant bacteria due to the overuse of antibiotics makes the pathogen clearance difficult, and has become a global threat that is expected to cause more deaths than all cancers combined by 2050[2, 3]. On the other hand, the regenerative environment is complex, thus requiring strong repair signals to accelerate bone remodeling. With the development of tissue engineering, studies have found that the process of bone healing is actively regulated by both biochemical signals (e.g., cytokines, growth factors and also essential trace elements required for bone healing) and biophysical signals (e.g., surface topography, local stiffness and compressive forces)[4–6]. Therefore, it is necessary to develop a biomaterial that possesses biochemical and biophysical characteristics, but avoids the risk of inducing drug resistance, for the treatment of IBD.

On a biochemical level, the immune system can be activated by signals to enhance antibacterial responses[7], but only focusing on the pathogen, while ignoring the dynamic healing process, cannot achieve good therapeutic results[1, 8]. Spatiotemporally coordinated regulation of the healing process of IBD through novel biomaterials is an important approach to address this problem[9, 10]. Current spatiotemporal bone engineering strategies mainly focus on the development of a programmed delivery pattern to match physiological/pathological cascades[11, 12]. One of the principal strategies to

orchestrate tissue regeneration is based on the delivery of bioactive molecules. However, the effectiveness tends to decrease over time *in vivo* due to the suboptimal biodistribution of the released bioactive reagents and a reduction in their bioactivity due to enzymatic degradation[13, 14]. At the same time, these strategies have the disadvantages of high cost and complex production. In comparison, bioactive ions (e.g., calcium, silicon, copper, magnesium and cerium) have been found to exert long-term multifunctional effects that promote tissue regeneration, and they are relatively inexpensive and resistant to enzymatic hydrolysis[13, 15–17], suggesting that these ions can provide biochemical biomimetic signals that can be incorporated into the design of bioactive materials for regenerative purposes.

Copper, as an important micronutrient, participates in many important biological processes and exhibits excellent antibacterial, pro-angiogenic and osteogenic properties and hence its use heralds the “Copper Age” in tissue engineering[18–20]. The physiological effects of copper ions are dose-dependent. Specifically, high doses of copper ions exhibited antibacterial effects yet avoided the risk of drug resistance[21], while low doses of copper ions promoted tissue repair responses[22]. Therefore, in the complex physiological cascade of IBD, a "multi-dimensional" regulation based on the staged release of Cu^{2+} is a potential therapeutic approach. Due to the excellent drug-loading and controlled release capabilities of bioglass (BGs), as well as the regulatory potential of its own component[23, 24]. We hypothesize that the copper doped BGs (CuBGs) can achieve spatiotemporal regulation of IBD by releasing different biomimetic signals at different times. Specifically, in the early stage, the fast release of Cu^{2+} could play an antibacterial role and promotes macrophage M1-mediated early inflammation to assist in clearing pathogens; in the later stage, the sustained release of Ca^{2+} and Si^{2+} from BGs may cooperate with low concentrations of Cu^{2+} to regulate excessive inflammation, angiogenesis and osteogenesis.

From a biophysical point of view, application of scaffolds with good physical characteristics (including mechanical adaptability and enabling viscotaxis) to the defect site is crucial for tissue regeneration[4, 25]. Indeed, cells have been shown to sense the mechanical properties of their environment through a variety of mechanisms, including mechanoreceptors, local adhesions, and the actin cytoskeleton[26]. It has been reported that lower-stiffness scaffolds promoted adipose-derived stem/stromal cells adipogenesis while stiffer scaffolds favored their osteogenic commitment[27]. The use of stiffness-optimized hydrogels could also promote the polarization of immune cells toward a reparative phenotype[28]. In addition, the ability to adapt to the irregular shape of the defect site would be beneficial to the force conduction and local drug retention in bone repair[4], and the correct viscosity would enhance the signal conduction between cells and biomaterials, which would be beneficial to tissue repair[29].

Hydrogels have shown great potential to provide physiologically relevant microenvironments for cell proliferation and tissue regeneration[30], while also serving as carriers for controlled drug release[31]. They are injectable, biocompatible, biodegradable, self-healing, and adaptable to various cavity sizes and shapes, which facilitate their application in tissue engineering[30]. Unfortunately, injectable hydrogels usually have weak mechanical properties and poor stability, making them unable to withstand external forces, thus limiting their application in bone engineering[32]. To overcome these limitations,

photocrosslinked hydrogels[33], which usually initiate chain polymerization via free radicals or bioorthogonal click reactions to achieve *in situ* curing, have become attractive biomaterials[33, 34]. Such photocrosslinked hydrogels have better physical characteristics due to the balance between injectability and mechanical strength[35]. Therefore, combining photocrosslinked hydrogels and CuBGs to form a dual biophysical and biochemical signal regulation system may be a promising solution for the treatment of IBD.

Herein, based on the concept of “photo-controlled *in situ* hardening”, we developed a dual photoenhanced interpenetrating network (IPN) by combining CuBGs, Methacryloyl-modified silk fibroin (SilMA) and Methacryloyl-modified gelatin nanoparticles (MA-GNPs) that enabled the bottom-up assembly of materials from the nanometer to macroscopic scale (Fig. 1). The electrostatic interactions between the polymer matrix and CuBGs endow the composite hydrogel with improved interfacial compatibility between inorganic and organic matter. Before photocrosslinking, SilMA was combined as a liquid with a non-covalent crosslinked colloidal network with shear thinning and self-healing capabilities, generating a hybrid hydrogel with injectability, plasticity and self-healing properties. After photocrosslinking, the network formed by SilMA was tightly combined with the colloidal network, and the mechanical strength increased by nearly 10 times and could resist cyclic stress. This dual-photocrosslinked interpenetrating network mechanism endowed the composite hydrogel with greater physical adaptability than a single network. A rat IBD model was used to study the ability of the hybrid hydrogel to provide biochemical and biophysical signals. The hybrid hydrogel showed ideal adaptability to the local complex environment of bone defects. Meanwhile, by sequentially releasing Cu^{2+}, Ca^{2+}, and Si^{2+} biomimetic signals from CuBGs on demand, the hybrid hydrogel spatiotemporally coordinated antibacterial, immunomodulatory and bone remodeling events. Overall, the dual photo-enhanced hydrogel could potentially break the current bottleneck in the treatment of IBD.

2. Materials And Methods

2.1. Fabrication and characterization of scaffolds

2.1.1. Synthesis and characterization of the hybrid hydrogel

MA-GNPs were prepared using the procedure described by Diba et al[36], SilMA solution was prepared according to the method of Kim et al[37] and CuBGs ($95SiO_2$/2.5CaO/2.5CuO (in mol%)) was synthesized by a modified Stöber method[38]. The detailed steps are shown in the Supporting Information (SI). For the hybrid hydrogel, Following its loading into a luer-lock medical syringe, 1 ml of SilMA solution (either 10, 15, 20, or 25% w/v) containing the photo-initiator lithium phenyl(2,4,6-trimethylbenzoyl) phosphinate (LAP) (0.25% w/v) was combined with 120 mg freeze-dried MA-GNPs powder and 10 mg CuBGs powder in a separate syringe, and the resulting mixture was repeatedly extruded to produce hybrid hydrogels. The hydrogels containing SilMA, MA-GNPs, and CuBGs are referred to as SGC hydrogel, and the hydrogels containing only SilMA and MA-GNPs are referred to as SG hydrogel. The mixed hybrid hydrogel was then

exposed to UV light (30 mW/cm^2) at a distance of 5 cm for 30 s in order to cause photo-crosslinking. The morphology of the hybrid hydrogel was observed using Scanning electron microscopy (FEI, Quanta 450, USA), and the elements C, Ca, Si and Cu were quantified and their distributions obtained by Energy-dispersive x-ray spectroscopy (EDX) mapping. Specifically, the hydrogels were frozen and broken up at -80°C, and then the water was taken out by freeze-drying them. Then, gold was put on the cross sections of the hydrogel samples to make them more conductive.

2.1.2. FT-IR, Zeta potential, DLS and TEM

To study graft copolymerization reactions, Fourier transform infrared (FT-IR) spectroscopy was used to confirm the structure of SilMA, MA-GNPs and CuBGs (Frontier, PerkinElmer, Rodgau, UK). The Zeta potential was measured using a Zetasize® Nano-S instrument (Malvern Instruments Ltd.). SilMA, MA-GNPs and CuBGs were dispersed in HPEPS (5mM) and mixed in the ratio of 20:12:1. Dynamic light scattering (DLS; Zetasizer Nano-S, NanoBrook 90 Plus PLAS) was used to measure the average particle size. Different concentrations of NaCl (0, 1, 5 or 10 mM) were added to the solution to observe the particle size change. For TEM, The CuBGs and CuBGs/MA-GNPs were dispersed in ethanol and after sonication for 5 min, the dispersed suspensions were examined

2.1.3. Rheological and Mechanical tests

The rheological properties were assessed using a AR2000ex rheometer (DHR, TA Instruments, USA)) with a parallel plate (diameter 20 mm). The operating gap was 1 mm, and the temperature was set to 25°C. Creep tests were conducted at 5 Pa for 1 minute to measure gel deformation, and the constant stress was removed to detect the recovery. The shear failure test was carried out with 1 Hz shear frequency and strain ranging from 0.1 to 100% to assess the self-healing properties of the samples. The light curing process adopted time sweep, and the testing process used ultraviolet light curing with a frequency of 1 Hz. Hydrogels' shear-thinning behavior was measured by altering the shear rate from 0.1 s-1 to 100 s-1 and recording the resulting changes in viscosity. The universal testing machine was used for all mechanical tests. SI displays the detailed procedures.

Tensile tests were also used to examine the hydrogels' self-healing ability after being damaged. The hydrogel samples were cut into two pieces and then brought into direct contact. Five minutes after contacting, samples were observed.

2.1.4. Injecting, molding and printing tests

Rhodamine was added to the hydrogel to give it a red color, and the hydrogel was subsequently extruded for writing and extruded into molds with different shapes before UV crosslinking. The hydrogel was put into a syringe and printed using a 3D printer with a needle tip movement speed of 10 mm/s and an extrusion pressure of 500 kPa.

2.1.5. Equilibrium swelling and release behavior

Before being weighed, the hydrogels were lyophilized. After 24 hours in 3 ml of phosphate buffered solution (PBS; pH = 7.4), the hydrogels were weighed after they had swollen. Following this formula, we were able to determine the final swelling ratio of the hydrogel:

Swell ratio = (Ws - Wd)/Wd (1)

where Ws and Wd represent the weight of the swollen and the lyophilized gel, respectively.

To determine the amount of Cu^{2+} released from the hybrid hydrogel, 1g of SGC hydrogel was soaked in 5 mL of PBS at room temperature for 10 days. Two and a half milliliters of PBS were removed daily for analysis using an inductively coupled plasma-atomic emission spectrometer (ICP-AES, Vista AX, Varian, USA), and 2.5 mL of fresh PBS was added back into the immersion solution.

2.2. Antibacterial activity of the hybrid hydrogel

2.2.1. Agar assay, bacterial live and dead staining

1g hydrogels *w*ere incubated with *Staphylococcus aureus* or *Escherichia coli* ($1x10^6$ CFU/ml) in 5 ml of tryptic soy broth (TSB, Sigma, USA) at 37℃ for 12 hours with shaking to test their *in vitro* antibacterial activity. Then,100 μl of the TSB was placed on an agar plate after dilution, spread evenly and incubated at 37℃. Images of the plates were taken after 24 h, and the total number of colonies was counted using image J software. Bacterial viability after incubation with hydrogels was assessed using the Live/Dead BacLight® Bacterial Viability Kit (Thermo Fisher, USA). Detailed methods are described in SI.

2.2.2. *Biofilm assay of antibacterial activity*

Wells in a 48-well microtiter plate were inoculated with 500 μl of an overnight TSB culture of *E. coli* or *S. aureus* cells ($1x10^6$ CFU/ml) and incubated at 37°C for 48 h to develop a static biofilm. After a further incubation with hydrogels for 24 h, crystal violet (CV, 0.2% (w/v)) staining was used to quantify the bacteria in the biofilms. Detailed methods are described in SI.

2.2.3. Exploration of antibacterial mechanism of SGC hydrogel

After being incubated with *E. coli* or *S. aureus* cells ($1x10^6$ CFU/ml) at 37°C for 12 hours, the hydrogel samples were fixed in 2.5% glutaraldehyde overnight for SEM analysis. The ROS level of the bacteria incubated with the hydrogel was measured with the 2',7'-dichlorodihydrofluorescein diacetate (DCFH-DA) assay (Reactive Oxygen Species Assay Kit, cat#S0033; Beyotime) (see details in SI, section 1.7). The special type of ROS generated within the bacteria treated by SGC hydrogel was evaluated by Dihydroethidium (DHE, as probe to O_2-), HKPerox-2 (as probe to H_2O_2). Diaminofluorescein-FM (DAF-FM) staining was used to test the formation of NO. Briefly, after incubate *E. coli* or *S. aureus* with hydrogels, the suspend bacteria was collected and washed by PBS for 3 times. Then the collected samples were

incubated in PBS with 20 μM of each probe at 37 ℃ for 1 hr. 10 μl of incubated sample was added on glass slide after evenly resuspend and confocal laser microscope was used for further imaging.

2.3. In vitro cell culture study

Raw264.7 and HUVECs (ATCC, Manassas, USA) were incubated in a humidified incubator (37°C, 5% CO_2) with Dulbecco's Modified Eagle's Medium (DMEM, Corning, USA) supplemented with 1% penicillin-streptomycin (HyClone, USA) and 10% fetal bovine serum (FBS, Gibco, USA). MC3T3-E1 cells (ATCC, Manassas, USA) were incubated with Minimum Essential Medium Alpha (α-MEM, Corning, USA) supplemented with 1% penicillin-streptomycin and 10% FBS. To examine MC3T3-E1 osteo-differentiation, we supplemented the growth medium with dexamethasone (10 nM), L-ascorbic acid (50 g/mL), and β-glycerophosphate (10 mM) (osteogenic medium, OM). To stimulate macrophages and create an inflammatory environment, LPS (100 ng/ml) was added to the medium. 1g SGC hydrogel was immersed in 5ml of DMEM medium, and the culture medium at day 3 and 7 was collected for culturing Raw264.7.

2.3.1. Cell biocompatibility

The live/dead staining kit (Solarbio, China) and Cell Counting Kit-8 assay (CCK-8; Solarbio, China) were used to test the biocompatibility of the hydrogels. Detailed methods are described in SI.

2.3.2. Expression of inflammation, angiogenesis and osteogenesis related genes

Macrophage M1 markers (CD86, TNF-α, IL-6), M2 markers (CD206, TGF-β, Arg), markers of osteogenic differentiation (ALP, Runx2, OPN, OSX and COL-1) and markers of angiogenic differentiation (CD31, VEGF and ANG1) were assessed using quantitative realtime polymerase chain reaction (qRT-PCR) assays. The specific steps of the qRT-PCR and the primer sequences are described in SI.

2.3.3. Immunofluorescence staining

Cells were fixed with 4% PFA for 30 min, washed 3 times with PBS, and then treated with 0.2% Triton (Sigma, USA) for 10 min. Primary antibodies (iNOS, CD206; abcam) were used to incubate the cells for 12 hours at 4°C. Subsequently, cells were washed 3 times with PBS and then stained with secondary antibody Alexa Fluor 488/594 for 1 h at room temperature followed by nuclear staining with 4,6-diamidino-2-phenylindole (DAPI) for 10 min at room temperature. All samples were then examined using laser scanning confocal microscopy (LSCM, TCS.SP8, Leica, Germany).

2.3.4. Cell migration and tube formation angiogenesis assay

Cell migration was observed using Transwell (8 μm of pore size; Bilfil, China) to assess the recruitment of vascular endothelial cells by the hydrogel. After 24h of culture, cells migrating from the transwell chamber to the bottom were fixed and stained with 0.5% CV for 30 min. The vascularization capacity of the hydrogels was examined by seeding 2×10^4 HUVECs in a 24-well plate coated with Matrigel (BD Biosciences, NJ) and incubating them at 37°C for 12h. The cells were then stained with a calcein solution

(Solarbio, China) for 15 min. Finally, images were captured using an EVOS scanning system (EVOS FL, Thermo-Fisher, USA), and semi-quantitative analysis of cell movement rates was performed in ImageJ.

2.3.5. ALP and ARS staining

Cells were cultured in hydrogels in osteogenic medium and then stained with a BCIP/NBT alkaline phosphatase color development kit (Roche, Switzerland) after 7 days to determine the osteogenic activity of the MC3T3-E1cells. After 28 days culture with hydrogels in osteogenic medium, Alizarin Red staining was used to evaluate post-osteogenic mineralization. The images were captured using an EVOS system.

2.4. Animal surgery and in vivo assessment

2.4.1. Rat infected femur defect model

Ethics approval for all in-vivo studies was granted by the School of Stomatology at Chongqing Medical University, ensuring that all procedures followed ARRIVE standards. The rats were cultured at room temperature and fed separately with no limits. General anesthesia was carried out during all the surgical treatment and all the rats had received penicillin injection after surgery to avoid postoperative infection.

Male Sprague Dawley rats (250–300 g) were randomly divided into four groups: Blank group, Control group, SG hydrogel, and SGC hydrogel (n = 3). A full-thickness defect (1.8 mm in diameter, 5 mm in depth) was drilled into the articular surface of the femoral-patellar groove under isoflurane gas and local anesthesia with lidocaine. *S. aureus* cells (10 μl 1x10^7 CFU/ml) in the PBS were injected into the defect to simulate an infected bone defect. After injecting the hydrogel into the defect, UV (30 s) was used to crosslink the hydrogel. The knee joint capsule and skin were stitched together layer by layer after the ligaments have been repositioned. The rats were euthanized at 3 and 7 days, 4 and 8 weeks after implantation to collect samples from their knees. At 3 and 7 days, the tissue around the defect was excised and cultured in TSB for bacteria enumeration using the agar assay. At the same time, heart blood was collected for routine blood and biochemical tests.

2.4.2. Micro-CT analysis of bone defects

Extracted tissues were rinsed in PBS after being fixed in 4% PFA at 4°C for 48 hours. Before CT scanning at 70 kV and 112 A (vivaCT40, SCANCO Medical AG, Switzerland), the fixed tissue samples were soaked in ethanol for 30 minutes. Following the acquisition of CT scans, 3D images were reconstructed and assessed for bone volume/tissue volume (BV/TV), trabecular thickness (Tb.Th), trabecular separation (Tb.Sp) and trabecular number (Tb.N) at the site of the defect.

2.4.3. Histological analysis and semi-quantitively evaluation of bone defects

Femoral samples were decalcified with 10% EDTA solution for approximately 2 months at room temperature. The samples were processed through a dehydration gradient and paraffin embedded before 6 μm sections were obtained with a microtome. H&E staining and conventional immunofluorescence

using primary antibodies against F4/80 (a marker of macrophages), iNOS, CD206 (abcam), CD31, and Runx-2 were performed on the tissue samples (Santa Cruz, USA). Secondary antibodies (Zhongshan Jinqiao Biotechnology, China) and antifade mounting media containing 4',6-diamidino-2-phenylindole hydrochloride were then incubated with the tissue slices (DAPI, Beyotime Biotechnology, China). Antibodies were all used after being diluted with goat serum. At the site of the bone defect, a 0.5 mm x 1 mm rectangle was established as the region of interest.

2.5. Statistical analysis

Data are presented as means ± standard deviation. All experiments were repeated in triplicates. One-way or two-way analysis of variance (ANOVA) were used to assess the multiple comparisons by GraphPad Prism 7.0. Statistical significance level was set at $P < 0.05$, where ns means not significant. * p 0.05, ** p 0.01, *** p 0.001, **** p 0.0001.

3. Results And Discussions

3.1. Preparation of the hybrid hydrogel

Figure 2A shows a schematic diagram of the two-step fabrication process for obtaining the hybrid interpenetrating network hydrogels with SilMA, MA-GNPs and CuBGs In a nutshell, the first network is formed when the three primary components are rapidly mixed, inducing self-assembly via electrostatic interactions. Next, in the presence a photo-initiator (LAP), UV light is used to further enhance the crosslinking between the MA-GNP gel and SilMA network in the hydrogel.

Firstly, FT-IR were used to confirm the modification of GMA on SF and MA on GNPs (Fig. 2B) [36, 37]. Specifically, FT-IR spectra showed characteristic SilMA and MA-GNPS peaks of amide I, II and III at 1641, 1530, and 1240 cm^{-1} (Fig. 2B). CuBGs exhibited an inorganic amorphous structure. Furthermore, Zeta potential measurements revealed that SilMA and CuBGs were negatively charged, while MA-GNPs were positively charged (Fig. 2C). The combination of the three induced an electrostatic attraction in SGC (Fig. 2C). Electrostatic interaction in SGC was supported by DLS analysis of the particle size. After mixing the three components, the mixture started to assemble, gradually forming larger clusters (Fig. 2D). We observed, using TEM, that the CuBGs particle size was about 300 ~ 450 nm. After mixing CuBGs with MA-GNPs, we found that the MA-GNPs wrapped around the CuBGs (Fig. 2E). In addition, the clusters gradually became smaller after incubation with NaCl (Fig. 2F), which can disrupt ionic interactions[39], suggesting electrostatic interactions is one of the stabilizing forces in the SGC hydrogel. Poor interfacial compatibility between the polymer matrix and inorganic particles has been reported[40], which may lead to the disordered separation of CuBGs in hybrid hydrogels, thereby affecting their properties such as stability and mechanical properties. The electrostatic interactions in the SGC hybrid matrix would be beneficial to improve the interfacial compatibility between CuBGs and the polymer matrix.

For the hydrogel synthesis, we used gels with MA-GNP volume fractions higher than random close packing ($\phi_{RCP} \approx 0.64$), corresponding to a MA-GNP concentration of 12% w/v, ensuring the formation of

a dense colloidal network.[4] Since the change of SilMA concentration would have a large impact on the mechanical properties and injectability of the hydrogel[29], we investigated changes in the rheological properties of hydrogels with different SilMA concentrations. Creep tests indicated that hydrogels with SilMA concentrations of 10% and 15% showed defects in their structure after applying certain stresses and some internal stresses could not be released, which may affect the hydrogel strength after deformation (Fig. 2G). In contrast, the 20% and 25% SilMA systems exhibited better stress release. After structural damage, all hydrogels had good self-healing properties (Fig. 2H). In the contact experiment after cutting, the same results were observed (Fig. S1). Most notably, hydrogels with 10, 15, 20% SilMA had the characteristic of shear thinning (Fig. 2I). However, the 25% SilMA hydrogel had a decrease in viscosity at high shear rates due to its greater strength and viscosity, which drifts out of the test area during shear by centrifugal and frictional forces (Fig. 2I). This may be because SilMA, as a polymer, tends to aggregate thus reducing the performance of shear thinning. At the same time, we found that after photocrosslinking (Fig. S2) or increasing the concentration of SilMA (Fig. 2J), there was both an increase in G' and G". However, when the SilMA content was increased, light transmission through the material decreased, resulting in slow light curing. It was also reported that an increase in SilMA concentration also delayed its degradation[29]. Therefore, considering the balance between the mechanical strength, curing time and injectability required for clinical treatment, 20% w/v SilMA was used in further experiments.

The microstructures of the hydrogels were observed using scanning electron microscopy (SEM, Fig. 2K). SEM images showed that SilMA has a sparse porous structure and smooth surface, while MA-GNPs were closely packed spherical particles. The hybrid SGC hydrogel exhibited a porous network formed by the interconnection of SilMA and self-assembled MA-GNPs, suggesting a possible cohesive interaction between these two components. Meanwhile, The SEM-energy dispersive X-ray (SEM-EDX) elemental mapping of SGC hydrogel was recorded to identify the elemental composition, suggesting the uniform distribution of Cu Ca and Si elements in the SG hydrogel matrix (Fig. 2L). In this construct, the SGC hydrogel forms a reinforced structure, in which SilMA is like a "rebar" that provides structural integrity and certain mechanical strength, while the MA-GNPs is like "concrete”, to further enhance the mechanical strength while maintaining the dynamic properties. Compared with single-network gels formed by SilMA and MA-GNPs, the hybrid hydrogel had a significantly higher storage modulus (Fig. S3). The mechanism by which the dual network enhances the mechanical properties was demonstrated in our previous study[4]. Specifically, the gelatin colloid forms a continuous particle network concurrently with the polymer fibrous network, which provides improved injectability/formability of the resulting composite hydrogel, but also enhances toughness by enabling energy dissipation upon loading. Therefore, this SGC hybrid hydrogel with an interpenetrating network could exhibit excellent biophysical adaptability.

3.2. Characterization of the hybrid hydrogel

The injectability and malleability of hydrogels are important properties for clinical application. The SGC hybrid hydrogel exhibited good injectability and could be easily ejected from a syringe without causing needle clogging (Fig. 3A). The shape of the gel can be controlled by injecting the hydrogel into molds with different shapes, such as circle, rectangle and heart, which indicates that the hydrogel is adaptable and

can meet any shape requirements for irregular bone defects caused by fractures, tumors, or other bone diseases. Furthermore, 3D printing, an advanced bio-fabrication technique that can generate patient-specific scaffolds with highly complex geometries, has been widely explored for the rapid design and fabrication of hydrogels[41]. Here, we printed a highly complex organ structure, the ear. This further illustrates the clinical application prospects of SGC hydrogels.

Generally, good adhesive properties of a hydrogel enable it to adhere to the defect's surface acting as a physical barrier, thereby achieving a physical hemostatic effect, and good adhesion is also conducive to subsequent osseointegration[29]. Therefore, the adhesive properties of the SGC hydrogel were investigated by lap shear strength experiments (Fig. 3C). We found that the adhesive strength of the SGC hybrid hydrogel was significantly stronger than that of the single-network Sil-MA and MA-GNPs gels (Fig. 3C).

A hydrogel with suitable stiffness not only provides a stable environment for tissue regeneration, but also modulate cellular responses at the site of implantation[42]. As indicated above, the double network formed in the SGC hybrid increased the hydrogel's strength. The improvement in the mechanical strength of the hydrogel after photocrosslinking was investigated. As shown in Fig. 3D, the UV-treated SGC hydrogel retained its original shape after being compressed (under a 500 g weight) without showing any signs of damage. Compression tests further showed that the Young's modulus of SGC hydrogel with UV light curing was significantly (~ 10 times) higher than that of SGC hydrogel without UV treatment (Fig. 3E). More notably, the SGC hydrogel without light curing showed increasing deformation of the structure after 5 and 10 cycles of compression or tensile tests, while after light curing, the Young's modulus of the SGC hydrogel hardly changed after 10 compression cycles. (Fig. 3F-I, Fig. S4). Thus, the light-enhanced SGC hydrogel has enhanced mechanical properties and stability, which indicates that the hydrogel can resist external pressure well after implantation *in vivo* and withstand the mechanical microenvironment of the defect site. Meanwhile, compared with MA-GNP gels, SGC hydrogels exhibited a significantly higher swelling rate (Fig. 3J), which would be beneficial for the movement of nutrients to promote cell infiltration into the scaffolds. In summary, dual-photocrosslinked SGC hydrogel exhibited excellent biophysical characteristics including injectability, local shape adaptability, 3D printability, and enhanced adhesive and mechanical properties.

In addition, we studied the release Cu^{2+} ions from SGC as a source of biochemical signals. Unlike release from pure CuBGs, the release of Cu^{2+} from CuBGs loaded in the SGC hydrogel was lower and slower (Fig. 3I), which would avoid biotoxicity after application *in vivo*. Cu^{2+} exhibited a biphasic release pattern, specifically, in the early stage, copper ions were released rapidly, while in the later stage, the ions begin were released at a steady lower rate. Cu^{2+} is reported to have an antibacterial activity against Methicillin-resistant Staphylococcus aureus (MRSA) and *E. coli* at 1 ppm[43], and the optimal dose of Cu^{2+} to promote angiogenesis is about 0.7 ppm[44]. From our data, in the first three days, the concentration of copper ions released from the SGC hydrogel was > 1ppm, and from the fifth day, the release of copper ions was maintained at about 0.7ppm copper ions. The concentration of copper ions in this biphasic

release mode is in the concentration range required for antibacterial activity and angiogenesis, which will be beneficial to realize the spatiotemporal control of pathogen clearance and repair in the IBD healing process. There have been many efforts to construct a drug delivery system that mimics the physiological healing process, but the shortcomings of existing strategies are the complex multi-drug loading process and difficulty in maintaining drug activity. In comparison, strategies for single-drug concentration-dependent regulation could significantly simplify the preparation process and provide more controllable biological regulation functions[45].

3.3. Antibacterial activity of the SGC hydrogel

Persistent bacterial infection of bone defects could have serious consequences such as severe inflammation, local bone loss and destruction, and vascular injury. If bacteria could be killed and cleared in a timely fashion, it would help restore the disturbed bone immune microenvironment and greatly improve the treatment efficiency. The agar plate count method was used to assess the in vitro antibacterial activity of the SGC hydrogel against the pathogenic bacteria *S. aureus* and *E. coli* (Fig. 4A, B, Fig. S5). A large number of colonies on the gar plate demonstrated that the SG hydrogel possessed little bactericidal activity against *S. aureus* or *E. coli*. However, after culturing with the SGC hydrogel there was strong antibacterial activity against *S. aureus* and *E. coli*, with greater than 100-fold reduction in viable cells. Live/dead staining showed that the SGC hydrogel increased the number of damaged or dead bacteria, which supported the findings of plate count assays (Fig. 4B). In addition, one of the most important factors contributing to persistent drug resistant infections is the formation of bacterial biofilms, which prevent antimicrobials from coming into contact with bacteria, delaying the healing of infected bone defects. Biofilms on microtiter plate wells were quantified with CV staining. The well coverage and stain quantification showed that the SGC hydrogel reduced the amount of biofilm by about 70% compared to the control, no hydrogel, group (Fig. 4C). The results show that the SGC hydrogel can effectively inhibit and destroy bacterial biofilms.

To explore the antibacterial mechanism of the SGC hydrogel, we investigated the effect of SGC hydrogel treatment on reactive chemical species within the bacteria. It is known that Cu^{2+} ions can increase intracellular ROS by catalyzing Fenton chemistry and generating hydroxyl radicals, and the elevated ROS levels lead to bacterial oxidative damage[18]. Use of the DCFH-DA probe showed that the bacteria treated with the SGC hydrogel produced a large amount of ROS, while the control group and SG hydrogel group had very low ROS levels (Fig. 4D). Using DHE, a fluorescent probe for superoxide ions, and HKPerox-2, a green fluorescent probe with high selectivity and sensitivity for H_2O_2, we further confirmed the species of ROS (Fig. 4E, F). Thus, the SGC hydrogel facilitated the formation of superoxide ions and H_2O_2 inside the bacteria, suggesting that the Cu^{2+} ions, through multiple ROS generation pathways, strengthened the antibacterial effect. At the same time, surprisingly, the SGC hydrogel also induced the production of NO (Fig. S6), which may contribute to bacterial killing[46]. In addition, Cu^{2+} ions could reduce the potential difference across the membrane leading to membrane depolarization, and subsequently membrane leakage or even rupture[47]. From the SEM images, the bacterial cellular morphology in the control and SG groups were smooth, spherical (*S. aureus*) and rod-shaped (*E. coli*). Following SGC hydrogel

treatment, there were fewer bacteria present, and the surface became indented or wrinkled, which was a sign that the bacteria were starting to die (Fig. 4G). Therefore, according to these findings, the antibacterial mechanism of SGC hydrogels may be due to the induction of bacterial oxidative stress and membrane depolarization by the released Cu^{2+} ions. (Fig. 4H).

3.4. Biocompatibility of the hybrid hydrogel

The biocompatibility of the hydrogels was tested by culturing different cell lines (MC3T3-E1, Raw264.7, and HUVECs) with the hydrogels. No significant difference in cell viability was observed between the hydrogel-treated and control groups using live/dead staining or the CCK-8 assay, indicating that the hybrid hydrogel is biocompatible. (Fig. S7). This is because both SilMA and MA-GNPs are naturally derived and have good biocompatibility, and the loaded CuBGs had no obvious toxicity due to the slow-release effect of the hydrogel. In addition, although SilMA lacks specific sites for cell adhesion, MA-GNPs contains a large number of RGD sequences (tripeptide sequence of Arg-Gly-Asp), which would increase the adhesion ability of cells to SGC hydrogels and further promote cell proliferation[48].

3.5. Immunomodulation properties of the SGC hydrogel

Macrophages are innate immune cells that play a key role in immune regulation and antimicrobial immune response in bone defect healing[49]. They are prime candidates for immune regulation due to their heterogeneity and plasticity. Specifically, macrophages are highly plastic cells that can polarize into various phenotypes and fulfill different roles. These roles are classified as "classical activation" (M1 phenotype), which promotes inflammatory responses and bacterial clearance, and "alternative activation" (M2 phenotype), which promotes immune regulation and tissue remodeling[50]. In IBD, the formation of a bacterial biofilm together with introduced biomaterial can induce a “frustrated” state in macrophages[51], leading to a significantly reduced antibacterial capability, and a delayed M1-M2 transition which will cause chronic inflammation and delay the healing process. Therefore, rationally designing a biomaterial that can promote synergistic M1 antibacterial activity in the early stage of application and promote M1-M2 conversion in the later stage can be a good strategy for the treatment of IBD (Fig. 5A). In this study we observed the effect of SGC hydrogels on macrophages at different time points. PCR analysis showed that at day 3, the expression of CD86, TNFα, and IL-6 in the SGC + LPS hydrogel group was higher than that in the LPS and SG + LPS groups. However, at day 7, CD206, TGF-β and ARG had the highest expression in the SGC + LPS group (Fig. 5B). The results were confirmed by immunofluorescence staining, the expression of pro-inflammatory factors was high at day 3 day and decreased at day 7, while the expression of anti-inflammatory factors showed opposite trend (Fig. 5B). This phenomenon was encouraging as it fulfilled the aforementioned requirements for IBD healing.

Reports of the effect of CuBGs on macrophages are contradictory[52, 53], but this might be due to different doses of Cu^{2+} ions being used[24]. High concentrations of Cu^{2+} ions can promote the polarization of pro-inflammatory macrophages and enhance the immune response to clear pathogens by activating copper transporter 1 and copper transporter ATPase 1 (ATP7A)[54]. But, at the same time, some studies have found that low concentrations of Cu^{2+} ions promote the anti-inflammatory phenotype

of macrophages[55, 56]. Therefore, the bimodal release pattern of Cu^{2+} ions from the SGC hydrogel may achieve the spatiotemporal regulation of macrophages. In addition, BGs have been shown to promote the polarization of macrophages to the M2 phenotype by locally releasing active ions. For instance, Si ions released from BGs have been shown to inhibit the pro-inflammatory response activity of macrophages, and released Ca^{2+} targets the Wnt/β-catenin signaling pathway and IL-10 (M2 marker gene) transcription via calcium-sensing receptor (CaSR) activation in macrophages[24]. This would be beneficial to promote polarization to the macrophage M2 phenotype at later stages of IBD treatment. In summary, the SGC hydrogel may have spatiotemporal immunomodulatory capabilities through changing the ion concentrations in the local microenvironment.

3.6. Angiogenesis and osteogenesis promoted by the SGC hydrogel

Blood vessels supply bone tissue with essential nutrients, oxygen, growth factors and hormones. Likewise, the osseointegration and bone defect repair processes may be enhanced by the vascular supply within tissue engineered implants[57]. Therefore, we investigated the effect of the SGC hydrogel on angiogenesis. By measuring cell migration with Transwell plates, we found that the SGC hydrogel induced increased cell migration of HUVECs, which would support greater angiogenesis (Fig. 6A). Meanwhile, qPCR results indicated that angiogenic genes (CD31, ANG-1, and VEGF) were more highly expressed in the SGC hydrogel group (Fig. 6B). The tube formation assay was used to further explore the angiogenic ability of SGC hydrogels. More tubes were formed in the SGC hydrogel group than in the SG hydrogel group (Fig. 6C). Semi-quantitative analysis also revealed that the total length of tube branches as well as the number of tube nodes and branches were much larger in the SGC hydrogel group than in the other groups (Fig. 6D). These results suggest that the SGC hydrogel has the potential to induce angiogenesis.

It has been previously reported that BGs could promote angiogenesis through dissolution and release of Si and Ca^{2+} ions[58]. Also, Hypoxia-inducible factor-1a (HIF-1a), a major transcription factor regulating VEGF expression, can be accumulated and activated by Cu^{2+} ions due to their ability to inhibit prolyl hydroxylases.[53]. Therefore, the incorporation of Cu^{2+} ions into BGs could further enhance the angiogenic ability. Indeed, according to our release results (Fig. 3K), the concentration of Cu^{2+} ions released by the SGC hydrogel is maintained at about 0.7 ppm, the optimum angiogenesis-promoting concentration, which will be beneficial to the tissue repair process. Therefore, it is likely that the SGC hydrogel possesses pro-angiogenic ability due to the sustained release of pro-angiogenic biomimetic signals.

In the early stages of osteogenic differentiation, alkaline phosphatase (ALP) is a useful marker. As shown in Fig. 6E, the SGC hydrogel induced more ALP expression on day 7 than the SG hydrogel. In addition, mineralization in the late osteogenic differentiation stage was determined by Alizarin Red staining. The most calcium nodules were observed with the SGC hydrogel (Fig. 6F). Gene expression assays for ALP, RUNX2, OSX, OPN and COL-1 were subsequently performed to determine the molecular effects of the

hydrogel on cell differentiation (Fig. 6G). The highest ALP gene expression was seen in the SGC hydrogel group at day 7, OSX and RUNX2 were highly expressed at day 7 and day 14, OPN and COL-1 were highly expressed in the SGC group on day 14. These results indicate that the SGC hydrogel has the ability to enhance osteogenesis. It has been reported that during the process of osteogenic differentiation, osteogenesis-related genes are expressed in a certain order[59], in which ALP is the gene expressed in early osteogenesis, OSX and RUNX2 are the genes expressed in the early and middle stages, and OPN and COL-1 are the genes expressed in late osteogenesis. The expression of osteogenic genes regulated by the SGC hydrogel is in line with this physiological expression sequence. Thus, the SGC hydrogel promoted the programmed expression of osteogenic genes through spatiotemporal regulation (Fig. 6H).

Since their introduction, BGs have found widespread application in the field of bone regeneration and repair. As BGs degrade, a silicon-rich layer forms on their surface; this layer encourages the formation of hydroxyapatite (HA) and tightly combines with collagen fibers produced by osteoblasts[60]. Furthermore, leached ions such as Ca^{2+} and Si stimulate osteoprogenitor cells at the genetic level and endow BGs with good osteoconductivity and osteoinductivity. Moreover, Cu^{2+} ions, as divalent cations, have been shown to promote bone formation by activating skeleton interoception and downregulating sympathetic tone[61]. Therefore, the SGC hydrogel could release a variety of biomimetic signals from CuBGs to promote bone formation. From a biophysical point of view, as mentioned before, mechanically enhanced hydrogels are more conducive to osteogenesis, compared to other hydrogels. Indeed, the SG hydrogel, without CuBGs, also induced cell migration and had higher ALP expression than the control in the early stage, which might indicate that the enhanced biophysical characteristics of the SC hydrogels could promote osteogenesis (Fig. 6I). Therefore, the ability of SGC hydrogels to promote osteogenesis might be due to the synergistic effect of biochemical and biophysical signals.

3.7. In vivo therapeutic performance of the SGC hybrid hydrogel

The *in vivo* therapeutic potential of the SGC hybrid hydrogel was examined in a bacteria-infected femoral bone defect model. Following creation of the defect (1.8 mm diameter), saline was injected into the defects (blank group). *S. aureus*, a major cause of clinical bone infection, was injected into bone defects of the control group. In two other groups, the SG and SGC hydrogels were injected into the defects simultaneously with the injection of *S. aureus*, and the defects were irradiated with UV for 30 s. Treatment effects were assessed by observation and tissue collection at days 3 and 7, and weeks 4 and 8 (Fig. 7A).

When the defect was created, a large amount of blood oozed out of the defect. When the hydrogel was implanted, the bleeding did not improve significantly because the gel did not fit tightly in the defect (Fig. S8). However, after photocuring, the bleeding stopped. This indicated that the SGC hybrid hydrogel successfully sealed with the surrounding tissue. It is believed that the strong adhesive properties of the SGC hydrogel may be due to the mechanical interlocking generated by the covalent bonding of the free radicals generated during the photo-crosslinking process after the infiltration of the SGC solution in the irregular surface of the defect[29].

At day 3 and day 7 we extracted the surrounding tissue from the defects for bacterial culture (Fig. 7B). We found that there were almost no bacteria in the samples from the SGC hydrogel group, whereas there were still a lot of bacteria in the samples from the control and SG hydrogel group. Therefore, the *in vivo* results showed that the SGC hybrid hydrogel has long-lasting antibacterial activity. Meanwhile, we collected cardiac blood for routine blood cell counts (Fig. 7C) and blood biochemical tests (Fig. 7D) before sacrificing the rats. The blood biochemistry results showed that there were no significant differences in ALT, AST, BUN and CRE levels between the groups, indicating that the SGC hydrogel had no obvious biological toxicity. It is worth mentioning that the blood cell count results showed that on day 3, the number of activated immune cells such as leukocytes, neutrophils, lymphocytes and monocytes in the blood of the rats in the control and SG hydrogel group was lower than in the SGC hydrogel group, which might be due to immune suppression caused by bacterial proliferation. The higher number of activated immune cells in the SGC hydrogel group might be due to the release of high concentrations of ions that activated immune cells. In contrast, on day 7, immune cells were increased in the SG hydrogel and control groups, whereas they were decreased in the SGC hydrogel group. This might be due to the activation of the immune system by the persistent infection in the SG hydrogel and control groups, while in SGC hydrogel group, the bacteria had been significantly cleared, the inflammation was reduced, so the immune response of the body transitioned towards repair.

The role of macrophages in the healing of IBD has already been emphasized. Here, we used F4/80 and iNOS staining to identify M1 macrophages and F4/80 and CD206 expression to characterize M2 macrophages. Figure 7F and G show that in the Control group, iNOS expression was high while CD206 expression was low. This indicated that M1 to M2 macrophage transition was hindered. However, In the SGC hydrogel group, immunofluorescence staining showed that the expression of iNOS on day 3 and the expression of CD206 on day 7 was much greater compared to the other two groups, suggesting that the SGC hydrogel activated more M1 macrophages for pathogen clearance on day 3 but activated more M2 macrophages for tissue repair on day 7. Previous studies have found that at the onset of the physiological healing process, macrophages are polarized into a pro-inflammatory M1 phenotype for phagocytic clearance of pathogens[62]. The number of M1 macrophages decreased over time, and by day 4 post-injury, the M2 phenotype dominated, promoting cell proliferation and tissue repair. In the healing of IBD, the above transitions are disturbed due to persistent infection. However, we found that the SGC hydrogel could regulate the inflammatory microenvironment *in vivo*, stimulating the M1 polarization of macrophages during the early injury stage and M2 polarization of macrophages during the later stage, which fully matches the optimum physiological biological cascade reaction.

Micro-CT was performed at 4, and 8 weeks after generating and treating the defect, and the bone healing was first analyzed from a macroscopic perspective. As shown in the CT images and 3D reconstructed images (Fig. 8A, B), the new bone in the defect area showed a tendency to grow from the periphery to the center. By 4 weeks post of surgery, there was little bone around the defect in the control and SG hydrogel groups, and the density of the bone was indistinct, this may be due to the enhanced osteoclast response and the inhibition of osteogenic activity due to persistent infection. The bone content treated by SGC hydrogel was significantly higher than in the other groups. At week 8, only a few areas of new bone

covered the defects in the control and SG hydrogel groups, while at week 8 the new bone in the SGC hydrogel group covered almost the entire defect. Further measurements of microstructural parameters were used to quantify new bone formation (Fig. 8C). After 8 weeks, the SGC hydrogel group had a bone volume fraction (BV/TV (%)) of up to 54.73.1%, compared to 42.12.3% in the blank group, 14.44.1% in the control group, and 23.33.4% in the SG hydrogel group, as measured by quantitative analysis of micro-CT scans. Bone microarchitecture, in addition to bone volume, is thought to be a significant factor in determining bone mechanical strength. The increase in trabecular bone number (Tb.N) in the SGC hydrogel group (Fig. 8C) indicated significant bone formation. At same time, trabecular thickness (Tb.Th) was increased and trabecular space (Tb.Sp) was decreased in the SGC hydrogel group compared to the control and SG hydrogel group. To further verify the regulation of various biological events in the process of IBD healing by hydrogels from a microscopic aspect, histological examinations were performed by HE staining and immunofluorescence staining. HE staining showed new bone ingrowth at the edge of the defect (Fig. 8D). At week 4, the control and SG groups showed mainly bone destruction, with a small amount of bone tissue and a large amount of fibrous tissue connected to the defect. In the SGC hydrogel group, new bone grew in from the edge. By week 8, the bone defect in the SGC hydrogel group had largely healed (Fig. 8D). At week 4 and week 8, immunofluorescence staining of the defect areas for CD31 (angiogenesis marker) and Runx2 (osteogenesis marker) showed that both CD31 and Runx2 expression were elevated in the SGC hydrogel group, indicating that more blood vessels and bone formation (Fig. 8D, E).

Combining the *in vitro* and *in vivo* results, we confirmed that the SGC hydrogel has the ability to spatiotemporally meet the needs of biochemical and biophysical signals at different stages of IBD healing (Fig. 8F). At the time of implantation, due to the dual-photocrosslinking IPN of the SGC hydrogel, it could be cured *in situ* after injection and molding, and achieve physical hemostasis. Due to the excellent mechanical properties and stability, the SGC hydrogel could resist external pressure well after implantation *in vivo* and match the mechanical microenvironment of the defect site. This physical adaptability of the implanted biomaterial is thought to be critical for tissue regeneration. In addition, the rapid release of copper ions in the early stage of implantation is beneficial for the killing of bacteria, and for increasing the clearance of the pathogens by activating M1 macrophages. As changes in the ionic microenvironment increased the proportion of M2 macrophages, this multifunctional hydrogel could help suppress the inflammatory response and promote angiogenesis and tissue remodeling. Therefore, the above results demonstrated that SGC hydrogels have great promise for hastening the recovery from IBD.

4. Conclusion

In this study, a promising hybrid hydrogel with excellent biophysical adaptability was developed to promote rapid healing of IBD by spatiotemporally regulating the healing process. The hydrogel was composed of CuBGs, photo-crosslinked SilMA and MA-GNPs. To provide biophysical signals from the dual-photocrosslinked interpenetrating network formed by SilMA and MA-GNPs, the hydrogel could be reinforced *in situ* by UV irradiation. The cured hydrogel exhibited excellent biophysical properties, such as adhesion, adaptation to the irregular shape and desirable mechanical properties. To overcome the

biological cascade disorder in the healing process of IBD, this hydrogel achieved spatiotemporal regulation of the healing process of IBD by releasing different biochemical signals from CuBGs at different time points. It was demonstrated in treating IBD in rats that the SGC hydrogel could effectively kill bacteria and remove pathogens in the early stage of implantation and promote the polarization of macrophages to the M2 phenotype later, and finally promote angiogenesis and osteogenesis. Therefore, the SGC hydrogel is expected to provide a simple, minimally invasive and effective treatment for the repair of infected bone defects without exogenous addition of expensive biological factors or resistance-inducing antibacterial drugs. In summary, the novel SGC hydrogel is expected to become a new strategy for the clinical treatment of IBD.

Declarations

Author contribution

Tao Chen, Huanan Wang, and Ping Ji designed the work, Tao Chen, Ping Ji, Dize Li, Qiming Zhai and Si Wang provided funding support. Guangyu Jian, Dize Li, Xu Chen and Qiwei Ying conducted the investigation, analysis, and validation. Guangyu Jian and Dize Li prepared the original draft manuscript. Li Mei and Richard D. Cannon participated in the data analysis and edited the manuscript. Tao Chen, Huanan Wang, and Ping Ji directed the investigation and edited the manuscript. All authors reviewed the manuscript.

Funding

This work was supported by grants from the National Natural Science Foundation of China (32071362, 82201075, 82201059), Key International (Regional) Joint Research Program funded by National Natural Science Foundation of China (NSFC) (82220108019), the China Postdoctoral Science Foundation (2022TQ0395) and the Science Fund for Distinguished Young Scholars of Chongqing (CSTB2022NSCQ-JQX0012)

Conflict of interest

the authors declare no competing interests.

References

1. Cui Y, Liu H, Tian Y, Fan Y, Li S, Wang G, et al. Dual-functional composite scaffolds for inhibiting infection and promoting bone regeneration. Mater Today Bio. 2022;16:100409. https://doi.org/10.1016/j.mtbio.2022.100409.
2. MacLean RC, San Millan A. The evolution of antibiotic resistance. Science. 2019;365(6458):1082–3. https://doi.org/doi:10.1126/science.aax3879.
3. Avershina E, Shapovalova V, Shipulin G. Fighting Antibiotic Resistance in Hospital-Acquired Infections: Current State and Emerging Technologies in Disease Prevention, Diagnostics and

Therapy. Front Microbiol. 2021;12:707330. https://doi.org/10.3389/fmicb.2021.707330.

4. Mu Z, Chen K, Yuan S, Li Y, Huang Y, Wang C, et al. Gelatin Nanoparticle-Injectable Platelet-Rich Fibrin Double Network Hydrogels with Local Adaptability and Bioactivity for Enhanced Osteogenesis. Adv Healthc Mater. 2020;9(5):e1901469. https://doi.org/10.1002/adhm.201901469.
5. Du Y, Yu M, Lu W, Kong J. Three-dimensional (3D), macroporous, elastic, and biodegradable nanocomposite scaffold for in situ bone regeneration: Toward structural, biophysical, and biochemical cues integration. Composites Part B: Engineering. 2021;225. https://doi.org/10.1016/j.compositesb.2021.109270.
6. Cheng W, Ding Z, Zheng X, Lu Q, Kong X, Zhou X, et al. Injectable hydrogel systems with multiple biophysical and biochemical cues for bone regeneration. Biomater Sci. 2020;8(9):2537–48. https://doi.org/10.1039/d0bm00104j.
7. Yang Y, Zhang H, Komasa S, Morimoto Y, Sekino T, Kawazoe T, et al. UV/ozone irradiation manipulates immune response for antibacterial activity and bone regeneration on titanium. Mater Sci Eng C Mater Biol Appl. 2021;129:112377. https://doi.org/10.1016/j.msec.2021.112377.
8. Jin X, Xiong YH, Zhang XY, Wang R, Xing Y, Duan S, et al. Self-Adaptive Antibacterial Porous Implants with Sustainable Responses for Infected Bone Defect Therapy. Advanced Functional Materials. 2019;29(17). https://doi.org/10.1002/adfm.201807915.
9. Mei J, Zhou J, Kong L, Dai Y, Zhang X, Song W, et al. An injectable photo-cross-linking silk hydrogel system augments diabetic wound healing in orthopaedic surgery through spatiotemporal immunomodulation. J Nanobiotechnology. 2022;20(1):232. https://doi.org/10.1186/s12951-022-01414-9.
10. Shi M, Zhang P, Zhao Q, Shen K, Qiu Y, Xiao Y, et al. Dual Functional Monocytes Modulate Bactericidal and Anti-Inflammation Process for Severe Osteomyelitis Treatment. Small. 2020;16(4):e1905185. https://doi.org/10.1002/smll.201905185.
11. Gan J, Zhang X, Ma W, Zhao Y, Sun L. Antibacterial, adhesive, and MSC exosomes encapsulated microneedles with spatio-temporal variation functions for diabetic wound healing. Nano Today. 2022;47. https://doi.org/10.1016/j.nantod.2022.101630.
12. Lv Z, Hu T, Bian Y, Wang G, Wu Z, Li H, et al. A MgFe-LDH Nanosheet-Incorporated Smart Thermo-Responsive Hydrogel with Controllable Growth Factor Releasing Capability for Bone Regeneration. Adv Mater. 2022:e2206545. https://doi.org/10.1002/adma.202206545.
13. Tian B, Li X, Zhang J, Zhang M, Gan D, Deng D, et al. A 3D-printed molybdenum-containing scaffold exerts dual pro-osteogenic and anti-osteoclastogenic effects to facilitate alveolar bone repair. Int J Oral Sci. 2022;14(1):45. https://doi.org/10.1038/s41368-022-00195-z.
14. Chen FM, An Y, Zhang R, Zhang M. New insights into and novel applications of release technology for periodontal reconstructive therapies. J Control Release. 2011;149(2):92–110. https://doi.org/10.1016/j.jconrel.2010.10.021.
15. El-Fiqi A, Mandakhbayar N, Jo SB, Knowles JC, Lee JH, Kim HW. Nanotherapeutics for regeneration of degenerated tissue infected by bacteria through the multiple delivery of bioactive ions and growth

factor with antibacterial/angiogenic and osteogenic/odontogenic capacity. Bioact Mater. 2021;6(1):123–36. https://doi.org/10.1016/j.bioactmat.2020.07.010.

16. O'Neill E, Awale G, Daneshmandi L, Umerah O, Lo KW. The roles of ions on bone regeneration. Drug Discov Today. 2018;23(4):879–90. https://doi.org/10.1016/j.drudis.2018.01.049.
17. He Q, Yuan S, Tang H, Wang S, Mu Z, Li D, et al. Safeguarding Osteointegration in Diabetic Patients: A Potent “Chain Armor” Coating for Scavenging ROS and Macrophage Reprogramming in a Microenvironment-Responsive Manner. Advanced Functional Materials. 2021;31(31). https://doi.org/10.1002/adfm.202101611.
18. Ermini ML, Voliani V. Antimicrobial Nano-Agents: The Copper Age. ACS Nano. 2021;15(4):6008–29. https://doi.org/10.1021/acsnano.0c10756.
19. Jacobs A, Renaudin G, Forestier C, Nedelec JM, Descamps S. Biological properties of copper-doped biomaterials for orthopedic applications: A review of antibacterial, angiogenic and osteogenic aspects. Acta Biomater. 2020;117:21–39. https://doi.org/10.1016/j.actbio.2020.09.044.
20. Seo JJ, Mandakhbayar N, Kang MS, Yoon JY, Lee NH, Ahn J, et al. Antibacterial, proangiogenic, and osteopromotive nanoglass paste coordinates regenerative process following bacterial infection in hard tissue. Biomaterials. 2021;268:120593. https://doi.org/10.1016/j.biomaterials.2020.120593.
21. Li K, Xia C, Qiao Y, Liu X. Dose-response relationships between copper and its biocompatibility/antibacterial activities. J Trace Elem Med Biol. 2019;55:127–35. https://doi.org/10.1016/j.jtemb.2019.06.015.
22. Zhang J, Wu H, He F, Wu T, Zhou L, Ye J. Concentration-dependent osteogenic and angiogenic biological performances of calcium phosphate cement modified with copper ions. Mater Sci Eng C Mater Biol Appl. 2019;99:1199–212. https://doi.org/10.1016/j.msec.2019.02.042.
23. Vallet-Regi M, Salinas AJ. Mesoporous bioactive glasses for regenerative medicine. Mater Today Bio. 2021;11:100121. https://doi.org/10.1016/j.mtbio.2021.100121.
24. Zheng K, Niu W, Lei B, Boccaccini AR. Immunomodulatory bioactive glasses for tissue regeneration. Acta Biomater. 2021;133:168–86. https://doi.org/10.1016/j.actbio.2021.08.023.
25. Higuchi A, Ling QD, Chang Y, Hsu ST, Umezawa A. Physical cues of biomaterials guide stem cell differentiation fate. Chem Rev. 2013;113(5):3297–328. https://doi.org/10.1021/cr300426x.
26. Bakhshandeh B, Ranjbar N, Abbasi A, Amiri E, Abedi A, Mehrabi MR, et al. Recent progress in the manipulation of biochemical and biophysical cues for engineering functional tissues. Bioengineering & Translational Medicine. 2022. https://doi.org/10.1002/btm2.10383.
27. Xie J, Zhang D, Zhou C, Yuan Q, Ye L, Zhou X. Substrate elasticity regulates adipose-derived stromal cell differentiation towards osteogenesis and adipogenesis through beta-catenin transduction. Acta Biomater. 2018;79:83–95. https://doi.org/10.1016/j.actbio.2018.08.018.
28. Wang FY, Qiu T, Ling Y, Yang Y, Zhou Y. Physical and Chemical Cues at the Nano-Bio Interface for Immunomodulation. Angew Chem Int Ed Engl. 2022;61(41):e202209499. https://doi.org/10.1002/anie.202209499.

29. Wu X, Zhou M, Jiang F, Yin S, Lin S, Yang G, et al. Marginal sealing around integral bilayer scaffolds for repairing osteochondral defects based on photocurable silk hydrogels. Bioact Mater. 2021;6(11):3976–86. https://doi.org/10.1016/j.bioactmat.2021.04.005.
30. Correa S, Grosskopf AK, Lopez Hernandez H, Chan D, Yu AC, Stapleton LM, et al. Translational Applications of Hydrogels. Chem Rev. 2021;121(18):11385–457. https://doi.org/10.1021/acs.chemrev.0c01177.
31. Li J, Mooney DJ. Designing hydrogels for controlled drug delivery. Nat Rev Mater. 2016;1(12). https://doi.org/10.1038/natrevmats.2016.71.
32. Zhang YS, Khademhosseini A. Advances in engineering hydrogels. Science. 2017;356(6337). https://doi.org/10.1126/science.aaf3627.
33. Wang Y, Zhang S, Wang J. Photo-crosslinkable hydrogel and its biological applications. Chinese Chemical Letters. 2021;32(5):1603–14. https://doi.org/10.1016/j.cclet.2020.11.073.
34. Xue X, Hu Y, Wang S, Chen X, Jiang Y, Su J. Fabrication of physical and chemical crosslinked hydrogels for bone tissue engineering. Bioact Mater. 2022;12:327–39. https://doi.org/10.1016/j.bioactmat.2021.10.029.
35. Qian Y, Zheng Y, Jin J, Wu X, Xu K, Dai M, et al. Immunoregulation in Diabetic Wound Repair with a Photoenhanced Glycyrrhizic Acid Hydrogel Scaffold. Adv Mater. 2022;34(29):e2200521. https://doi.org/10.1002/adma.202200521.
36. Diba M, Koons GL, Bedell ML, Mikos AG. 3D printed colloidal biomaterials based on photo-reactive gelatin nanoparticles. Biomaterials. 2021;274:120871. https://doi.org/10.1016/j.biomaterials.2021.120871.
37. Kim SH, Yeon YK, Lee JM, Chao JR, Lee YJ, Seo YB, et al. Precisely printable and biocompatible silk fibroin bioink for digital light processing 3D printing. Nat Commun. 2018;9(1):1620. https://doi.org/10.1038/s41467-018-03759-y.
38. Zheng K, Dai X, Lu M, Huser N, Taccardi N, Boccaccini AR. Synthesis of copper-containing bioactive glass nanoparticles using a modified Stober method for biomedical applications. Colloids Surf B Biointerfaces. 2017;150:159–67. https://doi.org/10.1016/j.colsurfb.2016.11.016.
39. Han Y, Lin Z, Zhou J, Yun G, Guo R, Richardson JJ, et al. Polyphenol-Mediated Assembly of Proteins for Engineering Functional Materials. Angew Chem Int Ed Engl. 2020;59(36):15618–25. https://doi.org/10.1002/anie.202002089.
40. Montheil T, Echalier C, Martinez J, Subra G, Mehdi A. Inorganic polymerization: an attractive route to biocompatible hybrid hydrogels. J Mater Chem B. 2018;6(21):3434–48. https://doi.org/10.1039/c8tb00456k.
41. Li J, Wu C, Chu PK, Gelinsky M. 3D printing of hydrogels: Rational design strategies and emerging biomedical applications. Materials Science and Engineering: R: Reports. 2020;140. https://doi.org/10.1016/j.mser.2020.100543.
42. Sharma RI, Snedeker JG. Biochemical and biomechanical gradients for directed bone marrow stromal cell differentiation toward tendon and bone. Biomaterials. 2010;31(30):7695–704.

https://doi.org/10.1016/j.biomaterials.2010.06.046.

43. Jacobs A, Renaudin G, Charbonnel N, Nedelec JM, Forestier C, Descamps S. Copper-Doped Biphasic Calcium Phosphate Powders: Dopant Release, Cytotoxicity and Antibacterial Properties. Materials (Basel). 2021;14(9). https://doi.org/10.3390/ma14092393.
44. Kong N, Lin K, Li H, Chang J. Synergy effects of copper and silicon ions on stimulation of vascularization by copper-doped calcium silicate. J Mater Chem B. 2014;2(8):1100–10. https://doi.org/10.1039/c3tb21529f.
45. Xie W, Fu X, Tang F, Mo Y, Cheng J, Wang H, et al. Dose-dependent modulation effects of bioactive glass particles on macrophages and diabetic wound healing. J Mater Chem B. 2019;7(6):940–52. https://doi.org/10.1039/c8tb02938e.
46. Yang G, Wang DY, Liu Y, Huang F, Tian S, Ren Y, et al. In-biofilm generation of nitric oxide using a magnetically-targetable cascade-reaction container for eradication of infectious biofilms. Bioact Mater. 2022;14:321–34. https://doi.org/10.1016/j.bioactmat.2022.01.044.
47. Mitra D, Kang ET, Neoh KG. Antimicrobial Copper-Based Materials and Coatings: Potential Multifaceted Biomedical Applications. ACS Appl Mater Interfaces. 2020;12(19):21159–82. https://doi.org/10.1021/acsami.9b17815.
48. Zhang Q-C, Ding W, Ding S-L, Meng Q-B, Su D-H, Zhang T-W, et al. Robust bioactive protein-based screws with dual crosslinked network for internal bone fixation. Composites Part B: Engineering. 2022;238. https://doi.org/10.1016/j.compositesb.2022.109884.
49. Mills EL, Kelly B, Logan A, Costa ASH, Varma M, Bryant CE, et al. Succinate Dehydrogenase Supports Metabolic Repurposing of Mitochondria to Drive Inflammatory Macrophages. Cell. 2016;167(2):457 – 70 e13. https://doi.org/10.1016/j.cell.2016.08.064.
50. Shapouri-Moghaddam A, Mohammadian S, Vazini H, Taghadosi M, Esmaeili SA, Mardani F, et al. Macrophage plasticity, polarization, and function in health and disease. J Cell Physiol. 2018;233(9):6425–40. https://doi.org/10.1002/jcp.26429.
51. Rosenberg G, Riquelme S, Prince A, Avraham R. Immunometabolic crosstalk during bacterial infection. Nat Microbiol. 2022;7(4):497–507. https://doi.org/10.1038/s41564-022-01080-5.
52. Shi M, Chen Z, Farnaghi S, Friis T, Mao X, Xiao Y, et al. Copper-doped mesoporous silica nanospheres, a promising immunomodulatory agent for inducing osteogenesis. Acta Biomater. 2016;30:334–44. https://doi.org/10.1016/j.actbio.2015.11.033.
53. Zhou Y, Han S, Xiao L, Han P, Wang S, He J, et al. Accelerated host angiogenesis and immune responses by ion release from mesoporous bioactive glass. J Mater Chem B. 2018;6(20):3274–84. https://doi.org/10.1039/c8tb00683k.
54. Huang Q, Ouyang Z, Tan Y, Wu H, Liu Y. Activating macrophages for enhanced osteogenic and bactericidal performance by Cu ion release from micro/nano-topographical coating on a titanium substrate. Acta Biomater. 2019;100:415–26. https://doi.org/10.1016/j.actbio.2019.09.030.
55. Xu X, Lu Y, Li S, Guo S, He M, Luo K, et al. Copper-modified Ti6Al4V alloy fabricated by selective laser melting with pro-angiogenic and anti-inflammatory properties for potential guided bone regeneration

applications. Mater Sci Eng C Mater Biol Appl. 2018;90:198–210. https://doi.org/10.1016/j.msec.2018.04.046.

56. Diez-Tercero L, Delgado LM, Bosch-Rue E, Perez RA. Evaluation of the immunomodulatory effects of cobalt, copper and magnesium ions in a pro inflammatory environment. Sci Rep. 2021;11(1):11707. https://doi.org/10.1038/s41598-021-91070-0.
57. Huang J, Han Q, Cai M, Zhu J, Li L, Yu L, et al. Effect of Angiogenesis in Bone Tissue Engineering. Ann Biomed Eng. 2022;50(8):898–913. https://doi.org/10.1007/s10439-022-02970-9.
58. Polo-Montalvo A, Casarrubios L, Serrano MC, Sanvicente A, Feito MJ, Arcos D, et al. Effective Actions of Ion Release from Mesoporous Bioactive Glass and Macrophage Mediators on the Differentiation of Osteoprogenitor and Endothelial Progenitor Cells. Pharmaceutics. 2021;13(8). https://doi.org/10.3390/pharmaceutics13081152.
59. An J, Yang H, Zhang Q, Liu C, Zhao J, Zhang L, et al. Natural products for treatment of osteoporosis: The effects and mechanisms on promoting osteoblast-mediated bone formation. Life Sci. 2016;147:46–58. https://doi.org/10.1016/j.lfs.2016.01.024.
60. Kaur G, Pandey OP, Singh K, Homa D, Scott B, Pickrell G. A review of bioactive glasses: Their structure, properties, fabrication and apatite formation. J Biomed Mater Res A. 2014;102(1):254–74. https://doi.org/10.1002/jbm.a.34690.
61. Qiao W, Pan D, Zheng Y, Wu S, Liu X, Chen Z, et al. Divalent metal cations stimulate skeleton interoception for new bone formation in mouse injury models. Nat Commun. 2022;13(1):535. https://doi.org/10.1038/s41467-022-28203-0.
62. Zarubova J, Hasani-Sadrabadi MM, Ardehali R, Li S. Immunoengineering strategies to enhance vascularization and tissue regeneration. Adv Drug Deliv Rev. 2022;184:114233. https://doi.org/10.1016/j.addr.2022.114233.

Figures

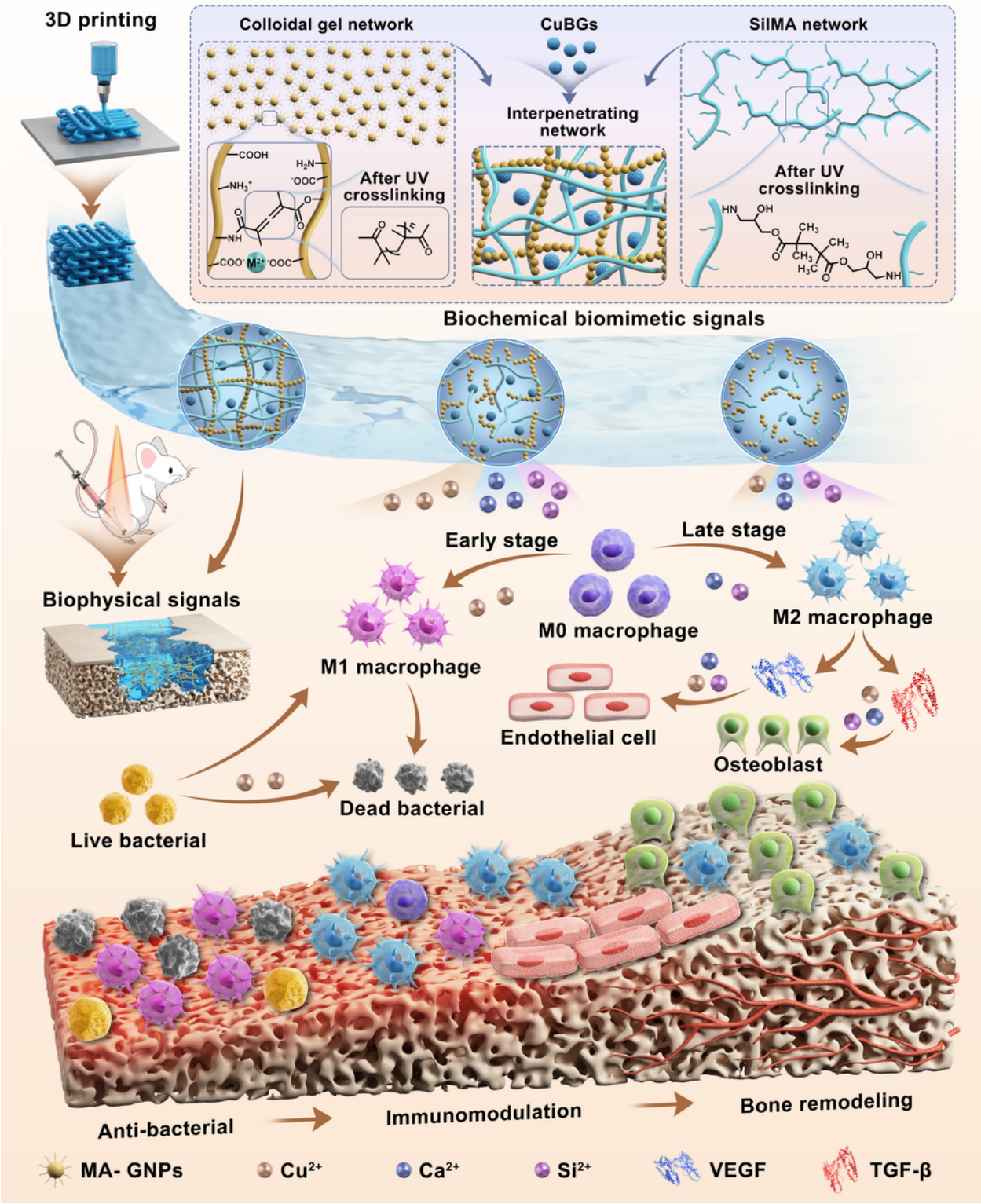

Figure 1

Schematic diagram showing the design principle of the hybrid hydrogel and the mechanism of the hybrid hydrogel induced infected bone defect regeneration through spatiotemporally regulating the healing process.

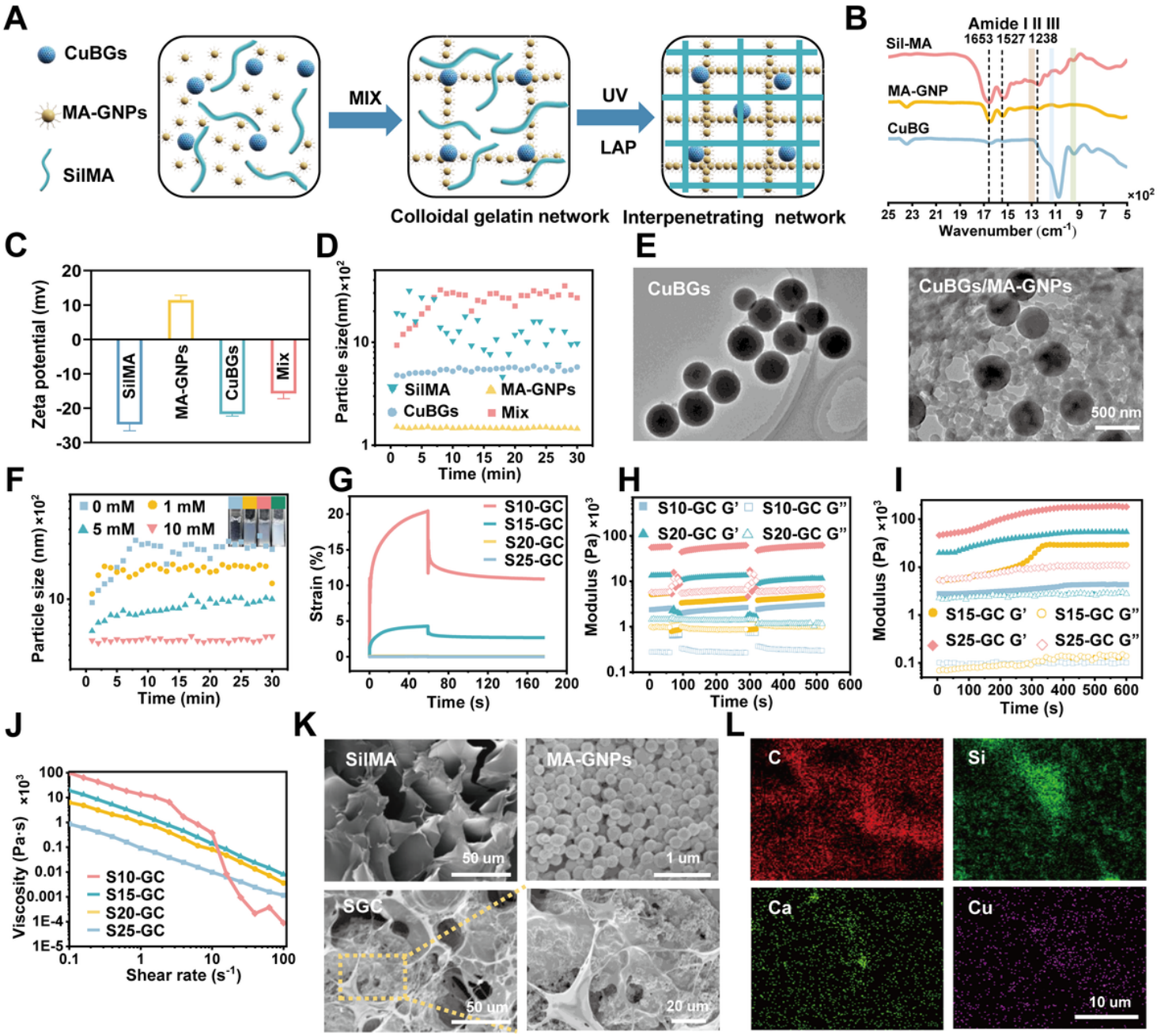

Figure 2

Synthesis of the SGC hydrogel. (**A**) Illustration of the formation of the interpenetrating polymer network within the hybrid hydrogel. (**B**) FT-IR spectra for freeze-dried SilMA, MA-GNPs and CuBGs. (**C**) The Zeta potential of CuBGs, SilMA, MA-GNPs and a mixture of the three. (**D**) The size of CuBGs, SilMA, MA-GNPs and a mixture of the three. (**E**) TEM image of CuBGs and a mixture of CuBGs and MA-GNPs. (**F**) The size of the SGC particles after incubation with different concentrations of NaCl. (**G**) Creep tests of hybrid hydrogels with different concentrations of SilMA. (**H**) Self-healing behavior of hydrogels with different concentrations of SilMA during destructive shearing and recovery. (**I**) Shear-thinning property of hydrogels with different concentrations of SilMA. (**J**) Time-dependent rheological studies of hybrid hydrogels with

different concentrations of SilMA. (**K**) SEM images of SilMA, MA-GNPs and SCG hydrogel. (**L**) EDX mapping of C, Si, Ca and Cu in SGC hydrogels.

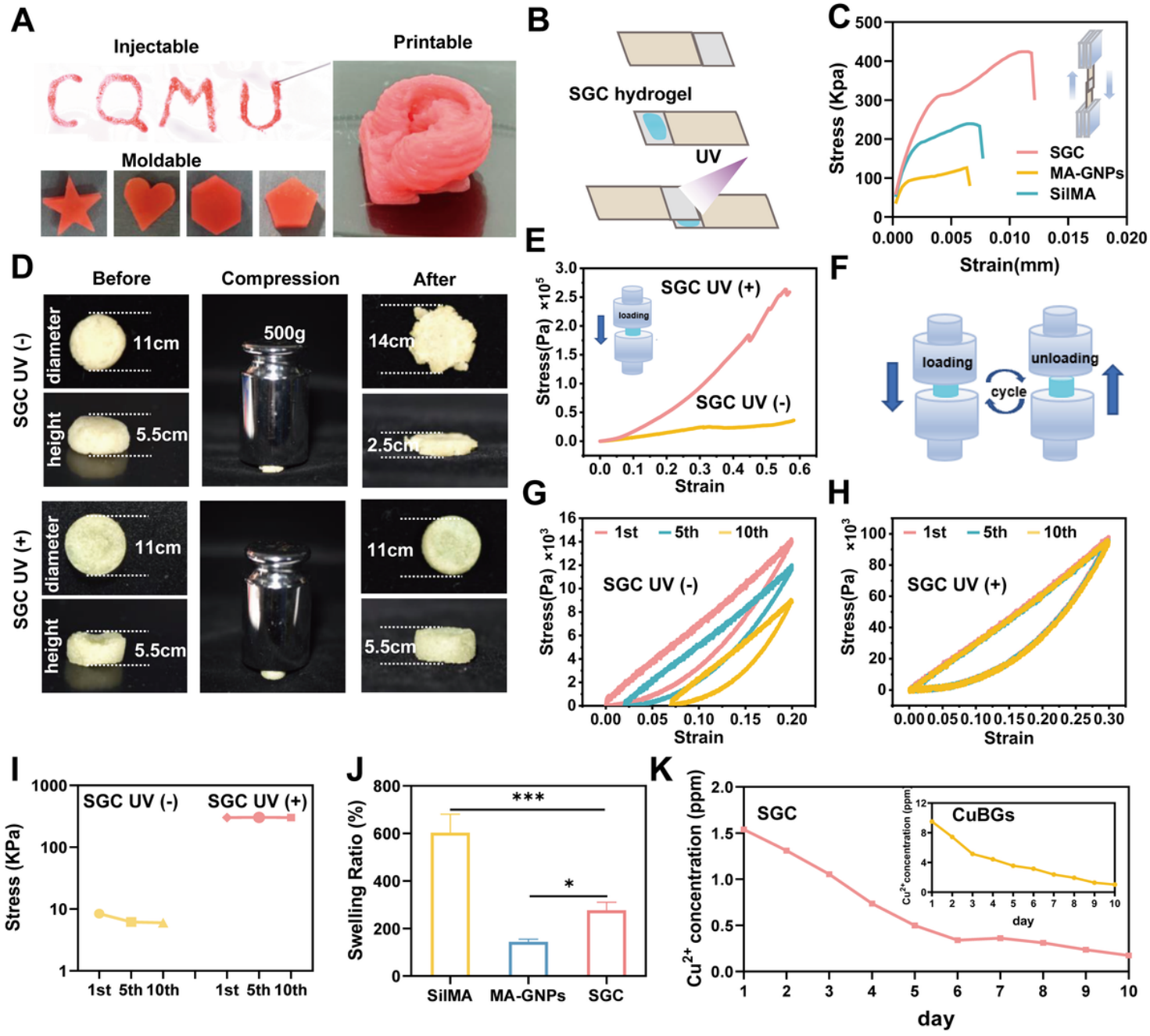

Figure 3

Physical adaptability of hydrogels. (**A**) Photographs of the injectability, moldability, and printability (image of an ear 3D printed using DLP printer) of the SGC hybrid hydrogel. (**B**) Schematic of the procedure for the measurement of lap shear strength. (**C**) Representative stress/strain curves of SGC, MA-GNP and SilMA hydrogels. (**D**) The SGC hydrogel with and without light-curing was compressed by a 500 g weight on the hydrogel for 30 s and the dimensions of the recovered hydrogels were measured. (**E**) Representative stress–strain curves for compression o the SGC hydrogels with and without light-curing.

(**F-I**) The hysteresis curves of the SGC hydrogels with and without light-curing upon cyclic compressive loading and unloading. (**J**) Equilibrium swelling study of hydrogels. (**K**) Concentration of Cu^{2+} released from pure CuBGs and SGC hydrogels over 10 days.

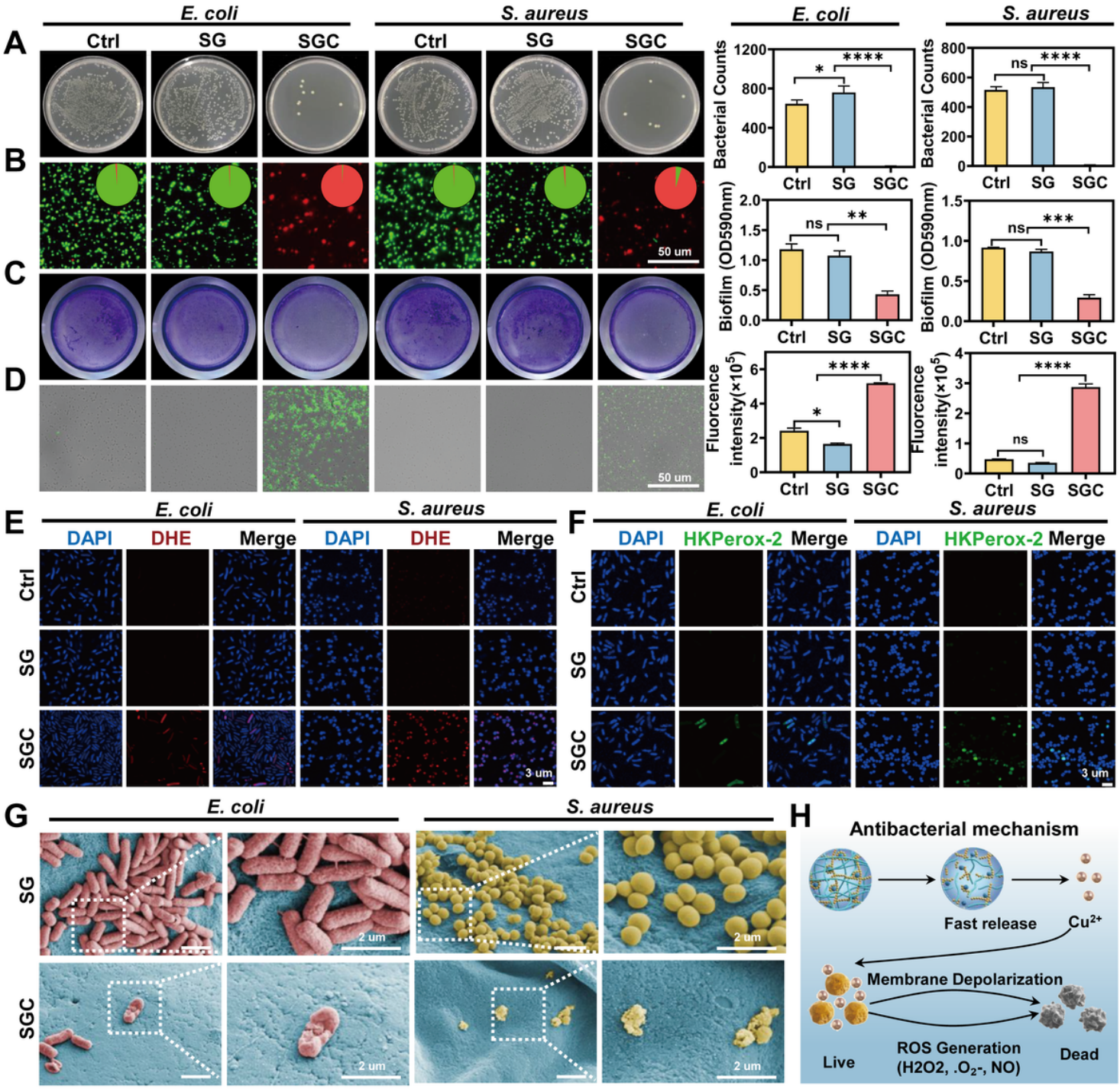

Figure 4

Antibacterial activity of the SGC hydrogel. (**A**) Agar plate assay of *S. aureus* and *E. coli* showing the antibacterial potential of SGC hydrogel. (**B**) Live/dead fluorescence images of *S. aureus* and *E. coli* after being incubated with the SG or the SGC hydrogel (Live/dead cells are stained green/red respectively). (**C**)

Crystal violet staining of bacterial biofilms incubated with the SG or the SGC hydrogel and percentage quantitative biofilm formation under different conditions (n = 3). (**D**) DCFH staining of bacteria showing the generation of ROS. (**E**) DHE staining of bacteria showing the formation of superoxide ions. (**F**) HKPerox-1 staining of bacteria showing the formation of H_2O_2. (**G**) Color enhanced SEM imaging of S. aureus and E. coli cultured on the surface of SG and SGC hydrogels. (**H**) Schematic diagram of the antibacterial mechanisms of the SGC hydrogel.

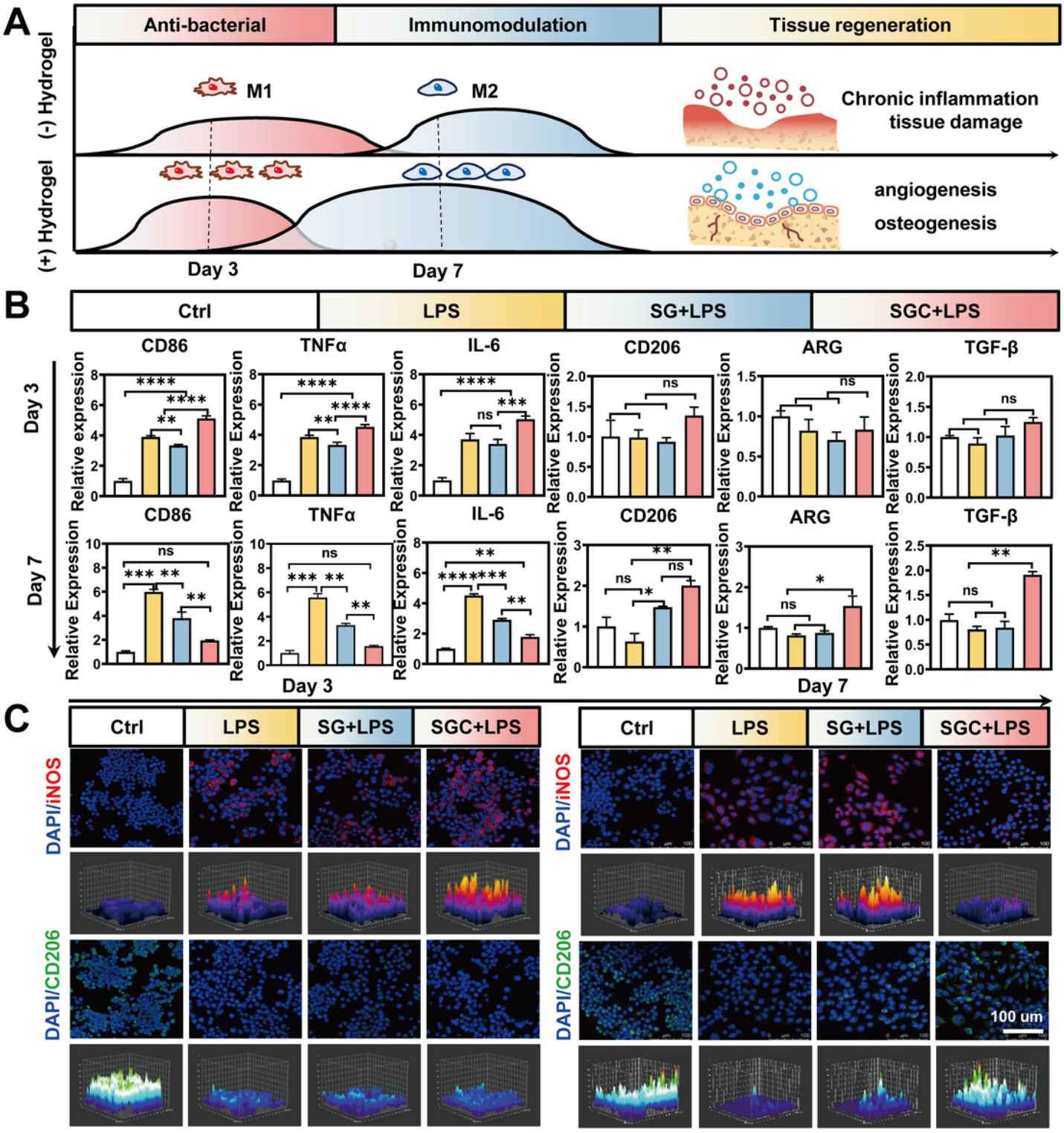

Figure 5

Macrophage polarization *in vitro* in response to the SGC hydrogels. (**A**) Schematic illustration of the effect of the SGC hydrogel on macrophage polarization and subsequent tissue repair. (**B**) Relative gene expression of M1 phenotype markers (CD86, TNF-α and IL-6) and M2 phenotype markers (CD206, ARG and TGF-β) in macrophages at day 3 and 7. (**C**) Representative fluorescence images of iNOS (red) and CD206 (green) staining of Raw264.7 cells after culture with hydrogels at day 3 and 7.

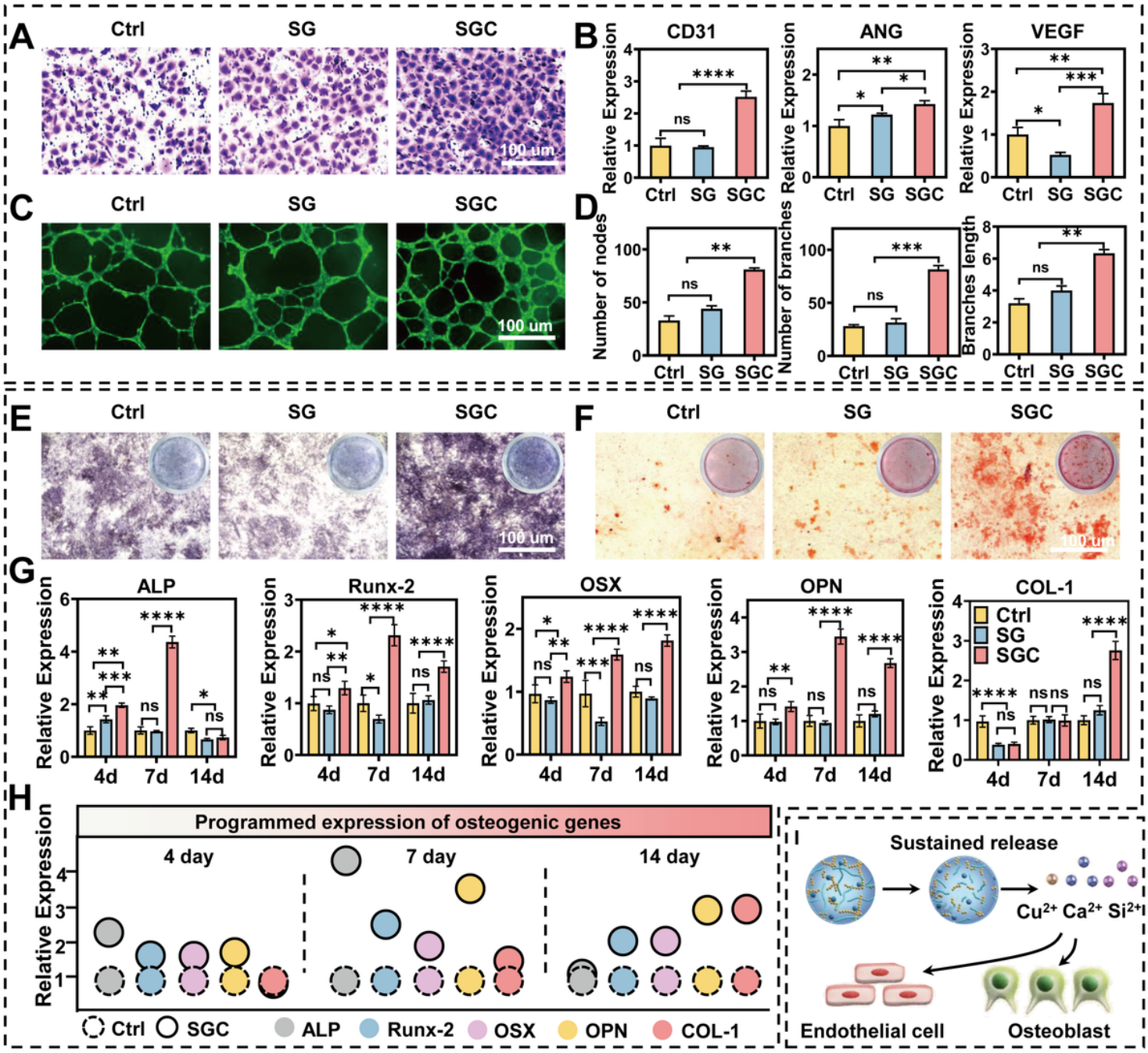

Figure 6

SGC hydrogel promoted angiogenesis and osteogenesis. (**A**) Analysis of HUVECs migration behavior using the Transwell assay with SG or SGC hydrogels. (**B**) Expression of angiogenesis-related genes CD31, ANG and VEGF determined by qRT-PCR on day 3. (**C**) HUVEC tube formation when cultured with SG or SGC hydrogels for 12h. (**D**) Semi-quantitative analysis of vascular tube formation (n = 3). (**E**) ALP staining on day 7 and (**F**) Alizarin red staining on day 28. The SGC hydrogels stimulated better osteogenesis. (**G**) qRT-PCR analysis of expression of osteogenesis-related genes (ALP, Runx2, OSX, OPN, COL-1) in cells cultured with the SG or SGC hydrogel. (**H**) The programmed expression of osteogenesis-related genes at different times induced by SGC hydrogel. (**I**) Schematic diagram of the angiogenesis and osteogenesis mechanisms induced by the SGC hydrogel.

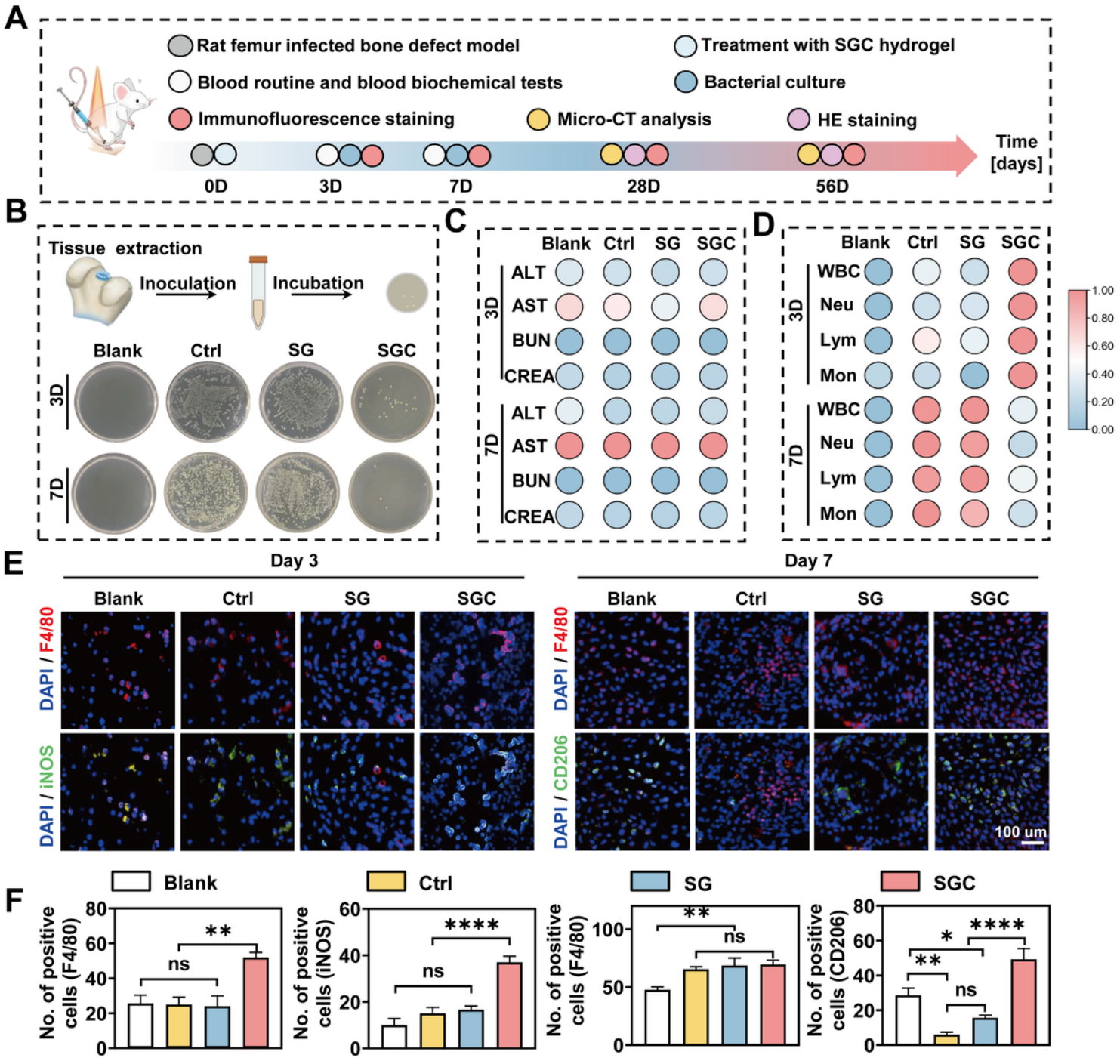

Figure 7

(**A**) Schematic diagram illustrating the timeframe of the *in vivo* study. (**B**) Schematic diagram showing the process of tissue sampling for bacterial analysis. Bacterial culture at day 3 and day 7, colony plate counts for the different groups. (**C**) Blood biochemical tests at day 3 and day 7 Routine blood cell counts at day 3 and day 7. (**D**) Routine blood cell counts at day 3 and day 7. (**E**) Representative fluorescent images showing the expression of macrophage marker F4/80 (red) and M1 marker iNOS (green) on day 3 and the expression of F4/80 (red) and M2 marker CD206 (green) on day 7 for infected bone defects. (**F**) Semi-quantitative analyses of the number of positive cells (F4/80, iNOS and CD206).

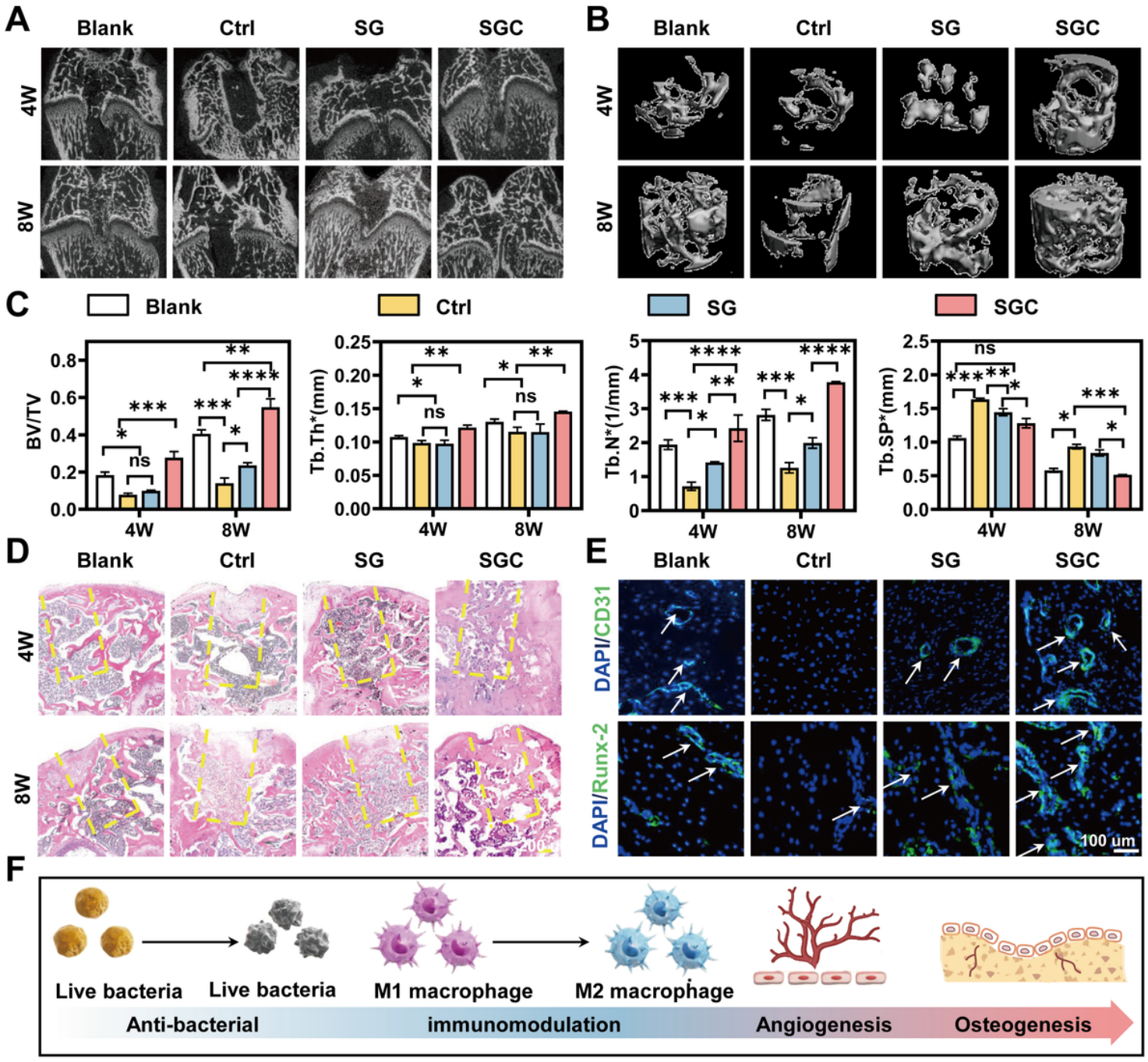

Figure 8

Histological evaluation of bone formation. (**A, B**) 3D images reconstructed from micro-CT analysis of hydrogels implanted in rabbit femurs for 4 and 8 weeks. (**C**) Quantification of bone volume/total volume (BV/TV) of defect, trabecular bone number (Tb.N), trabecular thickness (Tb.Th), and trabecular space (Tb.Sp). (**D**) Representative H&E staining images of defect area. (**E**) Representative immunofluorescence staining images showing the expression of CD31 (green) at week 4 and Runx2 (green) at week 8 in defect area. (**F**) Schematic diagram showing the spatiotemporal variation in the functions of the SGC hydrogel.

Supplementary Files

This is a list of supplementary files associated with this preprint. Click to download.

- SupplementaryInformation.docx